CHEMISTRY OF MATERIALS
Article

Chem. Mater. **2010,** *22,* 2517–2525 2517
DOI:10.1021/cm9031978

Atomic Layer Deposition of Ir−Pt Alloy Films

Steven T. Christensen and Jeffrey W. Elam*

Energy Systems Division, Argonne National Laboratory, Argonne, Illinois 60439

Received October 16, 2009. Revised Manuscript Received December 3, 2009

Atomic layer deposition (ALD) was used to prepare thin-film mixtures of iridium and platinum. By controlling the ratio between the iridium(III) acetylacetonate/oxygen cycles for Ir ALD and the (trimethyl)methylcyclopentadienyl platinum(IV)/oxygen cycles for Pt ALD, the Ir/Pt ratio in the films could be controlled precisely. We first examined the growth mechanisms for the pure Ir and Pt ALD films, as well as the mixed-metal Ir−Pt ALD films, using *in situ* quartz crystal microbalance and quadrupole mass spectrometer measurements. These studies revealed that the nucleation and growth of each of the noble metals proceeds smoothly, with negligible perturbation caused by the presence of the other metal. As a consequence of this mutual compatibility, the composition, as well as the growth per cycle for the Ir−Pt films, followed rule-of-mixtures formulas that were based on the ratio of the metal ALD cycles and the growth rates of pure Ir and Pt ALD. X-ray diffraction (XRD) measurements revealed that the films deposit as single-phase alloys in which the lattice parameter varies linearly with the composition. Similar to the pure noble-metal films, the Ir−Pt alloy films grow conformally on high-aspect-ratio trenches. This capability should open up new opportunities in microelectronics, catalysis, and other applications.

Introduction

Atomic layer deposition (ALD) is a thin-film synthesis technique in which both the thickness and composition can be precisely controlled at the atomic scale, which allows nanostructures to be engineered with relative ease.[1] The ALD of simple binary compounds and elements typically employs the sequential application of two precursor gases onto a solid surface, where the precursors chemically react separately in a self-limited fashion.[2] However, by expanding the ALD sequence to include additional precursors or pairs of precursors, ALD of mixed layers such as doped materials,[3−9] mixed oxides,[10−12]

*Author to whom correspondence should be addressed. E-mail: jelam@anl.gov.

(1) Knez, M.; Niesch, K.; Niinisto, L. Synthesis and surface engineering of complex nanostructures by atomic layer deposition. *Adv. Mater.* **2007**, *19*(21), 3425–3438.
(2) Ritala, M.; Asikainen, T.; Leskela, M. *Atomic Layer Deposition*; Academic Press: San Diego, CA, 2001; Vol. *1*.
(3) Suntola, T.; Jorma, A. Method for Producing Compound Thin Films. U.S. Patent 4,058,430, **1977**.
(4) Viirola, H.; Niinisto, L. Controlled growth of Sb-doped SnO_2 thin films by ALE. *Thin Solid Films* **1994**, *251*, 127–135.
(5) Kong, W.; Fogarty, J.; Solanki, R. ALE of ZnS:Tb thin film electroluminescent devices. *Appl. Phys. Lett.* **1994**, *65*(6), 670–672.
(6) Elers, K.-E.; Ritala, M.; Leskela, M.; Rauhala, E. $NbCl_5$ as a precursor for ALE. *Appl. Surf. Sci.* **1994**, *82/83*, 468–474.
(7) Jung, D.; Leonard, M.; El-Masry, N. E.; Bedair, S. M. Se doping of GaInP by ALE. *J. Electron. Mater.* **1995**, *24*(2), 75–78.
(8) Yousfi, E. B.; Weinberger, B.; Donsanti, F.; Cowache, P.; Lincot, D. ALD of ZnO and InS Layers for Cu(In,Ga)Se_2 Thin-Film Solar Cells. *Thin Solid Films* **2001**, *387*, 29–32.
(9) Elam, J. W.; Baker, D. A.; Martinson, A. B. F.; Pellin, M. J.; Hupp, J. T. Atomic layer deposition of indium tin oxide thin films using nonhalogenated precursors. *J. Phys. Chem. C* **2008**, *112*(6), 1938–1945.
(10) Nieminen, M.; Sajavaara, T.; Rauhala, E.; Putkonen, M.; Niinisto, L. Surface-controlled growth of $LaAlO_3$ thin films by ALE. *J. Mater. Chem.* **2001**, *11*, 2340–2345.
(11) Vehkamaki, M.; Hatanpaa, T.; Hanninen, T.; Ritala, M.; Leskela, M. Growth of $SrTiO_3$ and $BaTiO_3$ thin films by atomic layer deposition. *Electrochem. Solid State Lett.* **1999**, *2*(10), 504–506.
(12) Lie, M.; Nilsen, O.; Fjellvag, H.; Kjekshus, A. Growth of $La_{1-x}Sr_xFeO_3$ thin films by atomic layer deposition. *Dalton Trans.* **2009**, *3*, 481–489.
(13) Kattelus, H.; Ylilammi, M.; Saarilahti, J.; Antson, J.; Lindfors, S. Layered Ta-Al oxide films deposited by ALE. *Thin Solid Films* **1993**, *225*, 296–298.
(14) Kukli, K.; Ritala, M.; Leskela, M. Properties of ALD $TaNbO_x$ Solid Solution Films and Ta_2O_5−Nb_2O_5 Nanolaminates. *J. Appl. Phys.* **1999**, *86*(10), 5656–5662.
(15) Hartmann, J. M.; Charleux, M.; Mariette, H.; Rouviere, J. L. ALE of CdTe, MgTe and MnTe; growth of CdTe/MnTe tilted superlattices on vicinal surfaces. *Appl. Surf. Sci.* **1997**, *112*, 142–147.
(16) Ishii, M.; Iwai, S.; Kawata, H.; Ueki, T.; Aoyagi, Y. ALE of AlP and its applications to X-ray multilayer mirror. *J. Cryst. Growth* **1997**, *180*, 15–21.
(17) Kumagai, H.; Toyoda, K.; Kobayashi, K.; Obara, M.; Iimura, Y. TiO_2/Al_2O_3 Multilayer Reflectors for "Water-Window" Wavelengths. *Appl. Phys. Lett.* **1997**, *70*(18), 2338–2340.
(18) Elam, J. W.; Sechrist, Z. A.; George, S. M. ZnO/Al_2O_3 Nanolaminates Fabricated by Atomic Layer Deposition: Growth and Surface Roughness Measurements. *Thin Solid Films* **2002**, *414*, 43–55.
(19) Strømme, M.; Niklasson, G. A.; Ritala, M.; Leskela, M.; Kukli, K. $(Ta_{1-x}Nb_x)_2O_5$ films produced by atomic layer deposition: Temperature dependent dielectric spectroscopy and room-temperature *I*−*V* characteristics. *J. Appl. Phys.* **2001**, *90*(9), 4532–4542.
(20) Fujiwara, H.; Nabeta, T.; Kiryu, H.; Shimizu, I. Preparation and properties of $(ZnS)_3(ZnSe)_{42}$ ordered alloys fabricated by plasma-enhanced low-temperature growth technique. *Jpn. J. Appl. Phys., Part 1* **1994**, *33*(7B), 4381–4384.
(21) Mcdermott, B. T.; Reid, K. G.; Elmasry, N. A.; Bedair, S. M.; Duncan, W. M.; Yin, X.; Pollak, F. H. Atomic layer epitaxy of GaInP ordered alloy. *Appl. Phys. Lett.* **1990**, *56*(12), 1172–1174.
(22) Boutros, K. S.; Mcintosh, F. G.; Roberts, J. C.; Bedair, S. M.; Piner, E. L.; Elmasry, N. A. High quality InGaN films by atomic layer epitaxy. *Appl. Phys. Lett.* **1995**, *67*(13), 1856–1858.

Published on Web 03/02/2010

nanolaminates,[13−18] and alloys,[19−25] can be achieved. Most previous studies of mixed-layer ALD have focused on metal oxide and chalcogenide materials. The objective of these studies was to tune the composition of the metal oxide or chalcogenide layers to maximize the desired material properties such as charge storage capacity,[14] dielectric constant,[19] refractive index,[13] corrosion resistance,[26] or electrical conductivity.[27] However, there have only been a few reports on the ALD of mixed materials that contain metals, which, so far, are limited to mixtures with metal nitrides[28,29] or metal oxides.[30] There seem to be no studies yet regarding the ALD of mixed-metal layers. Applying the fine control afforded by ALD to mixed-metal films should open up new opportunities in microelectronics, catalysis, hydrogen storage, and medical applications. In particular, ALD has the potential to develop chemically enhanced metal nanolaminates, such as core−shell structures and near-surface alloys.[31]

During the ALD of mixed layers, the growth and properties of the films can often be predicted using simple rule-of-mixtures (RoM) formulas that are based on the precursor ratio employed during the deposition and the properties of the pure, constituent materials. These formulas assume that the growth of each of the components is unaffected by the presence of the other components in the film. However, there are many examples of ALD systems that do not follow RoM behavior, and this complicates the tasks of achieving a specific target film composition or predicting the film properties. Some reasons for this behavior include inhibited nucleation for one or more of the components[9,32] and etching of one component by the other.[32]

In this study, we investigate, for the first time, the ALD of mixed noble-metal layers. The ALD of mixed layers is practical only when the surface chemistries of the different components are mutually compatible and the deposition conditions are similar. In light of this, we have selected iridium and platinum as the materials for this initial study, because both can be prepared at 300 °C and they share oxygen as a common co-reactant. To deposit the Ir−Pt alloy films, we employ alternating exposures to iridium(III) acetylacetonate ($Ir(acac)_3$) and oxygen for the Ir component and alternating exposures to (trimethyl)-methylcyclopentadienyl platinum(IV) ($Pt(MeCp)Me_3$) and oxygen for the platinum component. The ALD of pure iridium and platinum films have been demonstrated with growth rates of ∼0.4 Å/cycle and ∼0.5 Å/cycle, respectively.[33,34] We control the composition of the Ir−Pt alloy films by adjusting the relative ratio of the $Ir(acac)_3/O_2$ and $Pt(MeCp)Me_3/O_2$ ALD cycles. We employ *in situ* quartz crystal microbalance (QCM) and quadrupole mass spectrometry (QMS) measurements to explore the growth mechanisms for the pure iridium and platinum metals and to examine the influence of the Ir−Pt cycle ratio on the film growth. The composition of Ir−Pt alloy films prepared on fused-quartz substrates is measured with X-ray fluorescence (XRF) and compared to film compositions deduced from the QCM results. We also perform scanning electron microscopy (SEM) to examine the morphology and conformality of the films on silicon and X-ray diffraction (XRD) to investigate the alloy structure and phase.

Experimental Details

ALD experiments were conducted in a viscous flow reactor[35] in which the deposition zone consisted of a stainless steel tube with a diameter of 5 cm. The QCM studies employed a Maxtek Model BSH-150 sensor head housing a single-side polished, AT-cut quartz crystal sensor (Colorado Crystal Corporation, Part No. CCAT1BK-1007-000) that was interfaced to a computer using a Maxtek Model TM400 film-thickness monitor. The reactor was heated using a multizone temperature-controlled exterior resistive heater system that maintained a constant reaction temperature. A constant flow of ultrahigh-purity (UHP, 99.999%) nitrogen carrier gas passed through the system at a rate of ∼360 sccm with a pressure of ∼1 Torr. Pressure was monitored using a capacitance manometer (MKS, Model Baratron 628B). The system incorporates an ozone generator (Pacific Ozone Technology, Model L11) for *in situ* substrate cleaning. The reactor is also equipped with a differentially pumped quadrupole mass spectrometer (Stanford Research Systems, Model RGA300) located downstream from the sample/QCM position and separated from the reactor by a 35-μm orifice.

The solid noble-metal ALD precursors were contained in separate stainless steel bubblers. The $Ir(acac)_3$ (Strem, 98%) was heated to 160 °C and the $Pt(MeCp)Me_3$ (Strem, 99%) was heated to 40 °C. The stainless steel tubing connecting the bubblers to the heated reactor manifold was heat-traced to

(23) Seim, H.; Molsa, H.; Nieminen, M.; Fjellvag, H.; Niinisto, L. Deposition of $LaNiO_3$ thin films in an atomic layer epitaxy reactor. *J. Mater. Chem.* **1997**, *7*(3), 449–454.
(24) Song, J. H.; Sim, E. D.; Baek, K. S.; Chang, S. K. Optical properties of ZnS_xSe_{1-x} ($x < 0.18$) random and ordered alloys grown by metallorganic atomic layer epitaxy. *J. Cryst. Growth* **2000**, *214*, 460–464.
(25) Schuisky, M.; Kukli, K.; Ritala, M.; Harsta, A.; Leskela, M. Atomic layer CVD in the Bi-Ti-O system. *Chem. Vapor Dep.* **2000**, *6*(3), 139–145.
(26) Matero, R.; Ritala, M.; Leskela, M.; Salo, T.; Aromaa, J.; Forsen, O. Atomic Layer Deposited Thin Films for Corrosion Protection. *Phys IV France* **1999**, *9*, 493–499.
(27) Elam, J. W.; Routkevitch, D.; George, S. M. Properties of ZnO/Al_2O_3 Alloy Films Grown Using Atomic Layer Deposition Techniques. J. Electrochem. Soc. **2003**, *150*, G339−G347.
(28) Kwon, S. H.; Kwon, O. K.; Min, J. S.; Kang, S. W. Plasma-enhanced atomic layer deposition of Ru-TiN thin films for copper diffusion barrier metals. *J. Electrochem. Soc.* **2006**, *153*(6), G578–G581.
(29) Kumar, S.; Greenslit, D.; Chakraborty, T.; Eisenbraun, E. T. Atomic layer deposition growth of a novel mixed-phase barrier for seedless copper electroplating applications. *J. Vacuum Sci. Technol. A* **2009**, *27*(3), 572–576.
(30) Sechrist, Z. A.; Fabreguette, F. H.; Heintz, O.; Phung, T. M.; Johnson, D. C.; George, S. M. Optimization and structural characterization of W/Al_2O_3 nanolaminates grown using atomic layer deposition techniques. *Chem. Mater.* **2005**, *17*(13), 3475–3485.
(31) Greeley, J.; Mavrikakis, M. Alloy catalysts designed from first principles. *Nat. Mater.* **2004**, *3*(11), 810–815.
(32) Elam, J. W.; George, S. M. Growth of ZnO/Al_2O_3 alloy films using atomic layer deposition techniques. *Chem. Mater.* **2003**, *15*(4), 1020–1028.
(33) Aaltonen, T.; Ritala, M.; Sammelselg, V.; Leskela, M. Atomic layer deposition of iridium thin films. *J. Electrochem. Soc.* **2004**, *151*(8), G489–G492.
(34) Aaltonen, T.; Ritala, M.; Sajavaara, T.; Keinonen, J.; Leskela, M. Atomic layer deposition of platinum thin films. *Chem. Mater.* **2003**, *15*(9), 1924–1928.
(35) Elam, J. W.; Groner, M. D.; George, S. M. Viscous flow reactor with quartz crystal microbalance for thin film growth by atomic layer deposition. *Rev. Sci. Instrum.* **2002**, *73*(8), 2981–2987.

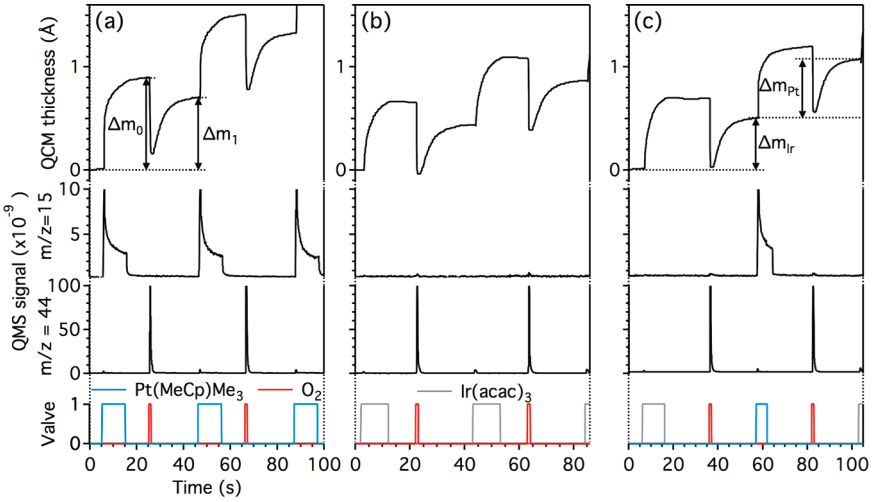

Figure 1. Synchronized QCM and QMS data for (a) Pt ALD, (b) Ir ALD, and (c) Ir−Pt mixed-metal ALD using a 1:1 $Ir(acac)_3$:$Pt(MeCp)Me_3$ cycles ratio. The bottom sections of the graphs show the precursor valve operation, where a value of 1 indicates that the respective precursor dosing valve is open. The QCM thickness trace for platinum in Figure 1a shows an increase during $Pt(MeCp)Me_3$ adsorption (Δm_0) and a smaller decrease from the O_2 dose to yield a net platinum thickness increase (denoted as Δm_1). In panel (c), the QCM thickness trace yields the net thickness increases from individual Ir ALD cycles (Δm_{Ir}) and Pt ALD cycles (Δm_{Pt}), which enable determination of the film composition. The QMS data are shown at mass-to-charge ratios of $m/z = 15$ for CH_4 and $m/z = 44$ for CO_2, which are the principle carbon-containing volatile byproducts of the ALD reactions.

prevent precursor condensation. During the precursor exposures, 60 sccm of the UHP N_2 carrier gas was diverted through the bubbler. Each ALD cycle consisted of an exposure to the metal precursor, a N_2 purge, an exposure to O_2, and a second N_2 purge. The optimized precursor exposure times were as follows: 7 s, $Ir(acac)_3$; 5 s, $Pt(MeCp)Me_3$; and 2 s, O_2. The QCM studies employed relatively long purge times of 20 s for the metal precursors and 10 s for the O_2 to allow the QCM signal to stabilize. When coating substrates, the purge times were reduced to 5 s for $Ir(acac)_3$, 2 s for $Pt(MeCp)Me_3$, and 2 s for O_2.

The substrates consisted of Si (100), fused quartz, and glass; all were 2−3 cm in size. Prior to deposition, the substrates were ultrasonically cleaned in acetone for 5 min, rinsed in isopropanol, and blown dry with N_2. After loading into the reactor, the substrates were allowed to outgas and thermally equilibrate for at least 10 min in flowing UHP N_2 at 300 °C and 1 Torr. Next, the substrates were cleaned *in situ*, using a 60-s exposure to 10% ozone in O_2 with a flow rate of 400 sccm at 300 °C. To improve the film uniformity, an ALD Al_2O_3 layer (1−5 nm) was deposited onto the substrates using alternating exposures to trimethylaluminum and water prior to the metal ALD. The ALD Al_2O_3 layer was deemed necessary after Ir films prepared on quartz without this layer were thinner than companion films prepared on the native oxide of silicon, indicating inhibited growth on the quartz surface.

The ALD Ir−Pt alloy films were characterized *ex situ* using X-ray fluorescence (XRF), SEM, and XRD. XRF measurements were performed on an energy-dispersive Oxford Instruments Model ED2000 system operated at 20 kV and 64 μA with an energy resolution of 140 eV. The composition and coverage were determined by comparing the count rate from the Lα lines of Ir and Pt for a fixed detector deadtime percentage. The XRF measurements were calibrated using pure Ir and Pt standards of known coverage, as determined by Rutherford backscattering spectrometry. XRD of ∼30 nm films was performed on a bending magnet station at Sector 5 of the Advanced Photon Source (Argonne, IL). The X-rays (E_γ = 16.015 keV; λ = 0.7742 Å) were focused in the transverse direction using a Kirkpatrick−Baez mirror, with a 2 mm × 0.5 mm incident beam slit, had an incident flux of $\sim 10^{10}$ photons/s, and were detected with a solid-state detector (Cyberstar). The X-ray energy was calibrated with the Si (004) Bragg reflection on a Si(001) substrate. Additional XRD experiments were conducted on a Rigaku Model ATXG rotating anode instrument using focused Cu Kα X-rays operated at 50 kV/240 mA, which produced a $\sim 10^8$ photon/s flux. The XRF and XRD measurements were performed on fused-quartz substrates where the quartz background was removed using data from a blank substrate. SEM secondary electron images were obtained using an Hitachi Model S4700 system with a field-emission gun operating at 5 kV.

Results and Discussion

***In Situ* Studies.** We performed *in situ* QCM and QMS measurements to explore the relationship between the ALD Ir−Pt growth and properties. Figure 1 shows *in situ* QCM and QMS measurements recorded during the ALD of Pt, Ir, and Ir−Pt mixed-metal films. For the mixed-metal films, we used an $Ir(acac)_3$:$Pt(MeCp)Me_3$ precursor dosing ratio of 1:1. Prior to recording each of these datasets, a sufficient number of ALD cycles were performed such that the QCM and QMS signals achieved steady-state values. The bottom traces in Figure 1 show the status of the precursor dosing valves, where a value of 1 indicates that the respective dosing valve is open. The top sections of Figure 1 show the QCM thickness values as a function of time. The QCM thickness values are calculated from the raw QCM signals, assuming densities of 22.56 g/cm^3 for Ir and 21.45 g/cm^3 for Pt. The middle traces show the QMS measurements at mass-to-charge ratios of $m/z = 44$ for CO_2 and $m/z = 15$ for CH_3 as a fragment of CH_4 obtained concurrently with the QCM data for the corresponding films. Rather than recording the $m/z = 16$ parent peak for CH_4, we recorded the $m/z = 15$ fragment to avoid interference from the large O_2 QMS signal at $m/z = 16$. The $m/z = 44$ data for each of the three ALD materials are shown on the same scale, so that differences in peak heights reflect differences in the

amounts of CO_2 released. Similarly, the $m/z = 15$ data are also shown on the same scale for each plot. The scale of the $m/z = 15$ data, relative to that of the $m/z = 44$ data, differs by an order of magnitude. To confirm that the QMS signals originate from reaction products formed in the higher-temperature regions of the reactor near the QCM, as opposed to the lower-temperature surfaces close to the QMS, we loaded the high-temperature portion of our reactor with steel wool to increase the surface area of this region by a factor of 10. We found that, while the magnitudes of the QMS signals were enhanced using the steel wool, the product ratios remained unchanged. This finding supports our assumption that the QMS and QCM sample the same process.

Platinum ALD. A previous *in situ* QMS investigation of Pt ALD using alternating exposures to $Pt(MeCp)Me_3$ and O_2 observed that CO_2 and H_2O were released as volatile byproducts during both the metal and oxygen precursor pulses.[36] The authors hypothesized that oxygen that had been adsorbed on the platinum film surface from the preceding O_2 exposure combusted some of the organic ligands during the $Pt(MeCp)Me_3$ exposure, and the remaining ligands were burned during the subsequent O_2 exposure. A larger fraction of the ligands were removed during the O_2 exposures compared to the $Pt(MeCp)Me_3$ exposures, but quantitative values were not given.

In a more recent examination[37] of Pt ALD using *in situ* gas-phase infrared (IR) spectroscopy, CH_4 was identified as a gas-phase product of the $Pt(MeCp)Me_3$ half-reaction in addition to the CO_2 and H_2O observed from both half-reactions. The CH_4 was assumed to result from ligand exchange reactions between the $Pt(MeCp)Me_3$ methyl ligands and reactive surface oxygen species such as hydroxyl groups. By quantifying the CO_2 and CH_4 signals, the authors deduced that ~13% of the carbon from $Pt(MeCp)Me_3$ was released during the metal precursor exposures with approximately equal amounts of CO_2 and CH_4, and the remaining 87% of the carbon was released during the O_2 exposures. Furthermore, *in situ* spectroscopic ellipsometry (SE) measurements exhibited a thickness increase during the $Pt(MeCp)Me_3$ exposures and a smaller thickness decrease during the O_2 exposures in qualitative agreement with the IR measurements.[37] However, the authors noted that their IR measurements were influenced by possible surface reactions on the colder walls (70 °C) of their ALD reactor and the SE measurements were not quantitative because they assumed a single dielectric function for both the platinum and the ligands. Consequently, we undertook a study of the Pt ALD mechanism using *in situ* QCM and QMS in our hot-walled ALD system (300 °C) to overcome some of these limitations.

We first conducted a systematic survey of the QMS signals during Pt ALD from $m/z = 2-100$ to identify the significant gas-phase reaction products. To boost our sensitivity at $m/z = 28$ for CO, we temporarily switched the carrier gas from nitrogen ($m/z = 28$) to argon ($m/z = 40$) but we observed no reaction products at $m/z = 28$. Furthermore, we did not observe methylcyclopentadiene as a reaction product with QMS. We found that $m/z = 15$ (fragment of CH_4), $m/z = 18$ (H_2O), and $m/z = 44$ (CO_2) were the only significant gas-phase reaction products during the Pt ALD. These byproducts are consistent with both of the aforementioned studies.[36,37] Because of the fact that we found no CO, we can assume that H_2O and CO_2 form in the ratio appropriate for complete combustion. To provide a reliable signature of the ligands released during Pt ALD, we focused our analysis on CO_2 and CH_4, because these volatile species are less likely to condense on surfaces downstream of the reaction zone in our ALD system, compared to H_2O.

Table 1. Integrated QMS Signals[a]

	CO_2 signal	CH_4 signal
$Pt(MeCp)Me_3$ pulse	1.96×10^{-9}	1.02×10^{-8}
O_2 pulse (Pt ALD)	4.59×10^{-8}	
$Ir(acac)_3$ pulse	2.01×10^{-9}	
O_2 pulse (Ir ALD)	4.53×10^{-8}	

[a] Values shown have a standard deviation of ±10%.

Coincident with the $Pt(MeCp)Me_3$ adsorption, the QMS signals in Figure 1a show a prominent peak at $m/z = 15$ and a small peak at $m/z = 44$, indicating that both CH_4 and CO_2 are released as reaction byproducts. During the subsequent O_2 exposures, CO_2 is the only volatile carbon-containing byproduct observed. The raw QMS signals were converted to CH_4 and CO_2 partial pressures by first subtracting the background QMS signals for these species measured during multiple $Pt(MeCp)Me_3$ or O_2 exposures.[38,39] Next, these signals were corrected for the relative QMS sensitivities and effusion rates into the pinhole[39] to obtain the partial pressures given in Table 1. Our results are in qualitative agreement with Kessels et al., in that a majority of the carbon is released during the O_2 exposures.[37] However, quantitatively, we find that 21% of the carbon is released during the $Pt(MeCp)Me_3$ exposures with the majority (18%) in the form of CH_4 and the minority (3%) in the form of CO_2, and the remaining 79% of the carbon is released during the subsequent O_2 exposures. This discrepancy may result from the aforementioned potential wall reactions in the previous study,[37] or from different O_2 partial pressures that may affect the surface chemistry of noble-metal ALD.[40] It is interesting that the CH_4 signal

(36) Aaltonen, T.; Rahtu, A.; Ritala, M.; Leskela, M. Reaction mechanism studies on atomic layer deposition of ruthenium and platinum. *Electrochem. Solid State Lett.* **2003**, *6*(9), C130–C133.
(37) Kessels, W. M. M.; Knoops, H. C. M.; Dielissen, S. A. F.; Mackus, A. J. M.; van de Sanden, M. C. M. Surface reactions during atomic layer deposition of Pt derived from gas phase infrared spectroscopy. Appl. Phys. Lett. **2009**, *95*, (1).
(38) Rahtu, A.; Alaranta, T.; Ritala, M. In Situ QCM and QMS Studies of ALD of Al_2O_3 from TMA and H_2O. *Langmuir* **2001**, *17*, 6506–6509.
(39) Elam, J. W.; Martinson, A. B. F.; Pellin, M. J.; Hupp, J. T. Atomic layer deposition of In_2O_3 using cyclopentadienyl indium: A new synthetic route to transparent conducting oxide films. *Chem. Mater.* **2006**, *18*(15), 3571–3578.
(40) Park, S. J.; Kim, W. H.; Maeng, W. J.; Yang, Y. S.; Park, C. G.; Kim, H.; Lee, K. N.; Jung, S. W.; Seong, W. K. Effect oxygen exposure on the quality of atomic layer deposition of ruthenium from bis(cyclopentadienyl)ruthenium and oxygen. *Thin Solid Films* **2008**, *516*(21), 7345–7349.

observed during the $Pt(MeCp)Me_3$ exposures appears (after background subtraction) as a broad, exponential decay extending for ~10 s, compared to the brief ~1−2 s spike for CO_2 during the O_2 exposures. This difference implies a much slower reaction during the $Pt(MeCp)Me_3$ exposures.

Given that $Pt(MeCp)Me_3$ has nine carbon atoms, the 18% carbon product released as CH_4 during the $Pt(MeCp)Me_3$ exposures for Pt ALD (Table 1) represents, on average, 1.6 C atoms. This CH_4 probably results from the reaction of methyl ligands on the $Pt(MeCp)Me_3$ molecule with surface functional groups. For instance, CH_4 is formed during Al_2O_3 ALD when methyl ligands on trimethyl aluminum react with surface hydroxyl groups.[38] It is understandable that the methyl ligands should react first during Pt ALD, given that methyl ligands are more reactive than cyclopentadienyl ligands in oxide ALD using heteroleptic compounds.[41,42] Hydroxyl groups have been observed previously on platinum surfaces exposed to oxidizing conditions[43] and the Pt−OH binding energy indicates that these hydroxyl groups should be stable at our deposition temperature of 300 °C.[44] The Pt−OH species on the Pt ALD surface may result from water released during the platinum precursor oxidation. The existence of surface hydroxyl groups on the ALD Pt surface could be confirmed using *in situ* Fourier transform infrared (FTIR) measurements.[45]

The top trace in Figure 1a shows the QCM thickness measurements during Pt ALD. These data yield a growth rate of 0.64 Å/cycle, which is somewhat larger than the 0.45 Å/cycle reported previously.[34,37] This discrepancy could be explained by a small amount of thermal decomposition during the relatively large $Pt(MeCp)Me_3$ exposures utilized in our experiments or by enhanced mass uptake due to a roughened QCM surface. The QCM data show a large thickness increase during the $Pt(MeCp)Me_3$ exposures, followed by a smaller thickness decrease during the O_2 exposures in qualitative agreement with the previous SE measurements.[37] The large, transient decrease in QCM thickness at the beginning of the O_2 exposures is attributed to the QCM thermal response to the heat released during the exothermic combustion reaction.[41] The absence of this feature during the $Pt(MeCp)Me_3$ exposures is consistent with the small CO_2 signals, indicating very little combustion. The net thickness decrease during the O_2 exposures supports the QMS observation that a majority of the carbon (79%) from the ligands on the $Pt(MeCp)Me_3$ molecule is removed during the O_2 exposures.

The QCM signals can be quantified using the QCM step ratio,[32,36,38] $\Delta m_1/\Delta m_0$, where Δm_0 is the thickness increase resulting from exposure to $Pt(MeCp)Me_3$ and Δm_1 is the net thickness change from one complete ALD cycle as displayed in Figure 1a. For Pt ALD, we obtain $\Delta m_1/\Delta m_0 = 0.79 \pm 0.01$, where the error bars show the standard deviation from measurements of multiple QCM steps. The predicted QCM step ratio is given by

$$\left(\frac{\Delta m_1}{\Delta m_0}\right)_{Pt} = \frac{M_{Pt}}{M_{Pt(MeCp)Me_3} - (x_{CH_4}M_{CH_4} + x_{CO_2}M_{CO_2} + x_{H_2O}M_{H_2O})} \quad (1)$$

where M_{Pt} is the atomic weight of platinum and $M_{Pt(MeCp)Me_3}$, M_{CH_4}, M_{CO_2}, and M_{H_2O} are the molecular weights of the corresponding molecules. The terms x_{CH_4} and x_{CO_2} represent the numbers of C atoms released from $Pt(MeCp)Me_3$ as CH_4 and CO_2, respectively, during the $Pt(MeCp)Me_3$ exposure. Finally, x_{H_2O} is the number of H_2O molecules released concurrently with the CO_2. From Table 1, we obtain $x_{CH_4} = 1.6$ and $x_{CO_2} = 0.3$. Assuming that the H_2O results from the complete combustion of the $Pt(MeCp)Me_3$ ligands (C_9H_{16}), $x_{H_2O} = {}^8/_9(x_{CO_2}) = 0.26$. Substituting these values into eq 1, we obtain the predicted value $\Delta m_1/\Delta m_0 = 0.74 \pm 0.07$, in excellent agreement with the QCM measurements (0.79 ± 0.01), which strengthens our proposed mechanism.

To summarize, our results suggest the following mechanism for Pt ALD: (1) $Pt(MeCp)Me_3$ reacts with adsorbed oxygen species on the Pt ALD surface, releasing 1.6 of the 3 methyl groups as CH_4 via ligand exchange and 0.3 methyl groups through combustion; (2) during the subsequent O_2 exposure, the remaining 1.1 methyl ligands and the methylcyclopentadienyl ligand are released by combustion and the platinum surface is repopulated with oxygen species.

Iridium ALD. The mechanism for Ir ALD has not been previously investigated but is thought to be comparable to that for Pt ALD and Ru ALD.[33] We can analyze the QCM and QMS data for Ir ALD in a manner similar to that previously described for Pt ALD. We first surveyed the QMS signals from $m/z = 2-100$ to identify the important gas-phase reaction products and found that only $m/z = 18$ (H_2O) and $m/z = 44$ (CO_2) were significant. The $m/z = 44$ trace in Figure 1b demonstrates that most of the CO_2 is released during the O_2 exposures with only a very small fraction released during $Ir(acac)_3$ adsorption. Although small peaks are seen at $m/z = 15$ during the O_2 exposures, this signal is merely a crack of the CO_2 and this trace is included only for comparison with the Pt ALD and Ir−Pt ALD.

(41) Elam, J. W.; Pellin, M. J. $GaPO_4$ sensors for gravimetric monitoring during atomic layer deposition at high temperatures. *Anal. Chem.* **2005**, *77*(11), 3531–3535.
(42) Jefimovs, K.; Vila-Comamala, J.; Pilvi, T.; Raabe, J.; Ritala, M.; David, C. Zone-doubling technique to produce ultrahigh-resolution X-ray optics. Phys. Rev. Lett. **2007**, *99* (26), No. 264801.
(43) Zhu, Y.; Dunn, K. A.; Kaloyeros, A. E. Properties of ultrathin platinum deposited by atomic layer deposition for nanoscale copper-metallization schemes. *J. Mater. Res.* **2007**, *22*(5), 1292–1298.
(44) Elam, J. W.; Zinovev, A.; Han, C. Y.; Wang, H. H.; Welp, U.; Hryn, J. N.; Pellin, M. J. Atomic layer deposition of palladium films on Al_2O_3 surfaces. *Thin Solid Films* **2006**, *515*(4), 1664–1673.
(45) Kim, S. K.; Lee, S. Y.; Lee, S. W.; Hwang, G. W.; Hwang, C. S.; Lee, J. W.; Jeong, J. Atomic layer deposition of Ru thin films using 2,4-(Dimethylpentadienyl)(ethylcyclopentadienyl)Ru by a liquid injection system. *J. Electrochem. Soc.* **2007**, *154*(2), D95–D101.

The raw QMS signals were converted to relative CO_2 partial pressures, as previously described, and the results are shown in Table 1. We first note that the CO_2 signals observed during the O_2 exposures for both the Pt ALD and Ir ALD are almost the same. We deduced that the CO_2 signal during the O_2 exposures for Pt ALD resulted from the combustion of 7.1 C atoms, and we can use this to calibrate the CO_2 signal during the Ir ALD. The atomic densities of Ir and Pt atoms deposited during each ALD cycle are 2.3×10^{14} and 3.5×10^{14}, respectively (see Figure 3, presented later in this work), so that the relative surface density for iridium is 0.67. Combining this quantity with the CO_2 partial pressures in Table 1 and the aforementioned calibration factor, we conclude that 10.5 C atoms are released during the O_2 exposures for Ir ALD. Because each acetylacetonate ligand has five C atoms, the QMS data indicate that two of the three acetylacetonate ligands are lost during the O_2 exposures and the remaining ligand is lost during the $Ir(acac)_3$ exposures.

If combustion occurred during both half-reactions, we would observe CO_2 QMS signals during the $Ir(acac)_3$ and the O_2 exposures in a 1:2 ratio. However, Table 1 shows only a tiny CO_2 signal during the $Ir(acac)_3$ exposures, accounting for just ~0.4 C atoms. Although we were unable to identify the major carbon-containing byproducts from the $Ir(acac)_3$ exposures, we suspect that this species is acetylacetone released by ligand exchange with surface hydroxyl groups, analogous to the CH_4 released during Pt ALD. To verify that our QMS is sensitive to acetylacetone, this compound was admitted into the reactor and we were able to detect this molecule. It is possible that, during Ir ALD, the acetylacetone forms slowly, resulting in a weak, broad QMS signal that is below our detection limit. Gas-phase IR absorption measurements could evaluate this possibility.

The QCM measurements for Ir ALD are shown as the top trace in Figure 1b. We observe a large thickness increase coincident with the $Ir(acac)_3$ exposures, and a smaller net thickness decrease during the O_2 exposures. As described previously, the transient thickness decrease during the O_2 exposures is most likely an artifact caused by the heat released during ligand combustion. The absence of such a feature during the $Ir(acac)_3$ exposures is further evidence that combustion does not occur. Our QCM measurements yield a growth rate of 0.46 Å/cycle, which compares very well with the growth rate of ~0.47 Å/cycle measured previously.[33]

Further details about the Ir ALD mechanism can be obtained from the QCM step ratio. Assuming ligand-exchange during the $Ir(acac)_3$ reaction, the QCM step ratio is

$$\left(\frac{\Delta m_1}{\Delta m_0}\right)_{Ir} = \frac{M_{Ir}}{M_{Ir(acac)_3} - x_{acac}(M_{acac} + 1)} \qquad (2)$$

where M_{Ir} is the atomic weight of iridium, $M_{Ir(acac)_3}$ and M_{acac} are the molecular weights of the corresponding molecules, and x_{acac} represents the number of acetylacetonate ligands lost during the $Ir(acac)_3$ exposures. Using the value of $\Delta m_1/\Delta m_0 = 0.67 \pm 0.01$ from QCM, eq 2 yields $x_{acac} = 2.0$, implying that ~2 acetylacetonate ligands are lost during the $Ir(acac)_3$ exposures. Taken together with the value of $x_{acac} = 1.0$ from QMS, our measurements suggest that ~50% of the acac ligands are released during the $Ir(acac)_3$ exposures.

To summarize, our results suggest the following mechanism for Ir ALD: (1) $Ir(acac)_3$ reacts with adsorbed oxygen species on the ALD Ir surface, releasing 1−2 of the acetylacetonate ligands through ligand exchange and ~0.1 ligand through combustion; (2) during the subsequent O_2 exposure, the remaining acetylacetonate ligands are released by combustion and the iridium surface is repopulated with oxygen species.

Mechanism for Iridium−Platinum Mixed-Metal ALD. Although the ALD of mixed-metal films has not been previously explored, we might expect some interaction between the different metals and ligands, which modifies the growth behavior, compared to the pure-metal ALD. Figure 1c presents the QCM and QMS measurements recorded during the ALD of Ir−Pt mixed-metal films using a $Pt(MeCp)Me_3$:$Ir(acac)_3$ dosing ratio of 1:1. This ratio was selected to amplify any nonideal behavior by forcing the surface chemistry to transition at every cycle. Remarkably, the QMS and QCM signals seem virtually unchanged for the Pt and Ir ALD cycles in the 1:1 mixed-metal film, compared to the corresponding signals for the pure metals. In particular, Figure 1c yields QCM step ratios of 0.81 ± 0.02 and 0.72 ± 0.03 for the Pt and Ir steps, respectively, in the 1:1 mixed-metal film, in close agreement with the values of 0.79 ± 0.01 and 0.67 ± 0.01 obtained during the pure Pt ALD and Ir ALD. Furthermore, the QMS signals for CH_4 and CO_2 in the 1:1 mixed-metal ratio are virtually identical to those observed for their pure-metal counterparts. We found similar behavior for a range of Ir−Pt mixed-metal films using $Pt(MeCp)Me_3$:$Ir(acac)_3$ dosing ratios of 1:10, 1:4, 1:1, 4:1, and 10:1. The fact that the QCM step ratios and QMS product distributions do not change for the Ir−Pt mixed-metal films demonstrates that the growth mechanisms for the platinum and iridium are not perturbed by the presence of the other metal. Consequently, we expect that the growth and composition of the mixed-metal films should follow RoM predictions.

Film Thickness Measurements. The thickness change between the start of the $Ir(acac)_3$ pulse and the subsequent $Pt(MeCp)Me_3$ pulse is denoted by Δm_{Ir} in Figure 1 and gives the net change in iridium thickness. Similarly, the net change in platinum thickness is given by Δm_{Pt}. By calculating the net change in thickness from each individual cycle and plotting versus the number of ALD cycles, we obtain the data in Figure 2. Figure 2 shows the *in situ* growth measurements for a range of ALD Ir−Pt alloy films prepared using 0%, 10%, 25%, 50%, 75%, 90%, and 100% $Ir(acac)_3$ cycles. Qualitatively, Figure 2 shows that platinum deposits faster than iridium and that the growth per cycle varies monotonically with the ratio of metal precursor pulses. The crosses in Figure 3 plot

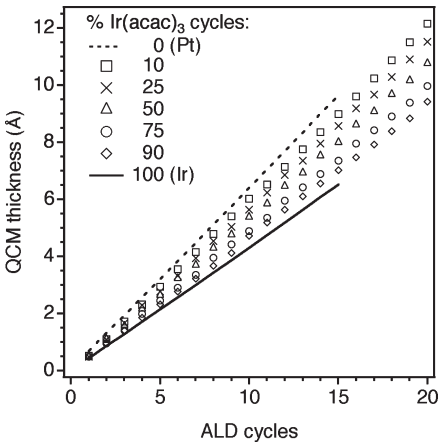

Figure 2. QCM thickness data for a series of ALD noble-metal films. The ALD growth per cycle is obtained from the slope of these curves and decreases as the percentage of $Ir(acac)_3$ cycles increases.

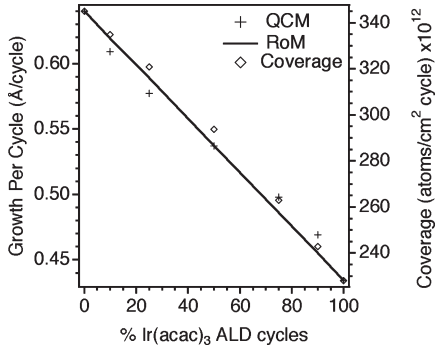

Figure 3. QCM growth per cycle and XRF metal atom coverage per cycle as a function of the percentage of $Ir(acac)_3$ cycles. The data agree well with the rule of mixtures (RoM) for film thickness (denoted by the solid line) given by eq 3.

the slopes of the growth curves in Figure 2 against the percentage of $Ir(acac)_3$ ALD cycles. Figure 3 also includes the predicted growth per cycle (solid line) based on a rule of mixtures:

$$G = f_{Ir}g_{Ir} + (1 - f_{Ir})g_{Pt} \quad (3)$$

where G is the growth per cycle, f_{Ir} the fraction of $Ir(acac)_3$ cycles, and g the respective growth per cycle for the pure iridium or platinum films. Figure 3 demonstrates that the thickness measurements agree very well with the RoM formula described by eq 3.

The diamond-shaped symbols in Figure 3 represent the growth per cycle of the ALD Ir−Pt alloy films derived from *ex situ* XRF measurements of samples prepared on silicon substrates coated first with ~5 nm of ALD Al_2O_3. The XRF thickness measurements were divided by the number of ALD cycles performed to obtain the growth per cycle. The *ex situ* XRF coverage measurements exhibit a linear trend that is similar to that of the *in situ* QCM thickness measurements. This agreement lends support to each of these measurement techniques. Previous studies of the growth of ALD mixed material films have reported large departures from RoM predictions in certain cases, because of nonideal behavior such as inhibited growth[9] and etching[32] upon transitioning between the different ALD materials. The excellent agreement between the XRF and QCM film growth measurements and the RoM formula in Figure 3 suggests that both the Ir ALD and Pt ALD grow equally well on either metal surface, as predicted by our *in situ* studies. Evidently, nonideal processes such as inhibited growth, surface poisoning, and etching do not occur.

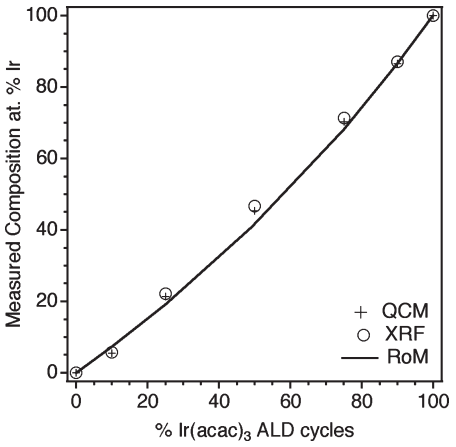

Figure 4. Film composition deduced from QCM and XRF measurements, as a function of the percentage of $Ir(acac)_3$ cycles. The data agree well with the rule of mixtures for film composition (denoted by a solid line) that is given by eq 6.

Composition Analysis. The compositions of the ALD noble-metal films were determined using both *in situ* QCM and *ex situ* XRF measurements performed on films deposited on Si(001) and quartz substrates that were first coated using 1−5 nm of ALD Al_2O_3. Figure 4 plots the iridium concentration against the percentage of $Ir(acac)_3$ cycles used to grow the film. The QCM composition is obtained by first calculating the thickness changes for the individual Ir (Δm_{Ir}) and Pt (Δm_{Pt}) cycles and then applying the following formula:

$$\text{Ir(QCM)}\ (\%) = \frac{\Delta m_{Ir}\rho_{Ir}}{\Delta m_{Ir}\rho_{Ir} + \Delta m_{Pt}\rho_{Pt}} \times 100 \quad (4)$$

where ρ refers to the density of the respective element. The XRF composition is obtained using the coverages of iridium (c_{Ir}) and platinum (c_{Pt}) determined from XRF measurements of the ALD Ir−Pt films, using the following expression:

$$\text{Ir(XRF)}\ (\%) = \frac{c_{Ir}}{c_{Ir} + c_{Pt}} \times 100 \quad (5)$$

Figure 4 also plots the RoM formula:

$$\text{Ir}\ (\%) = \frac{f_{Ir}\rho_{Ir}g_{Ir}}{f_{Ir}\rho_{Ir}g_{Ir} + (1 - f_{Ir})\rho_{Pt}g_{Pt}} \times 100 \quad (6)$$

where g is the growth per cycle for the indicated material. Fitting this model to the data gives growth-per-cycle values of g_{Ir} = 0.46 Å/cycle and g_{Pt} = 0.60 Å/cycle. These values agree very well with the values of 0.43 Å/cycle and 0.64 Å/cycle that have been obtained by QCM

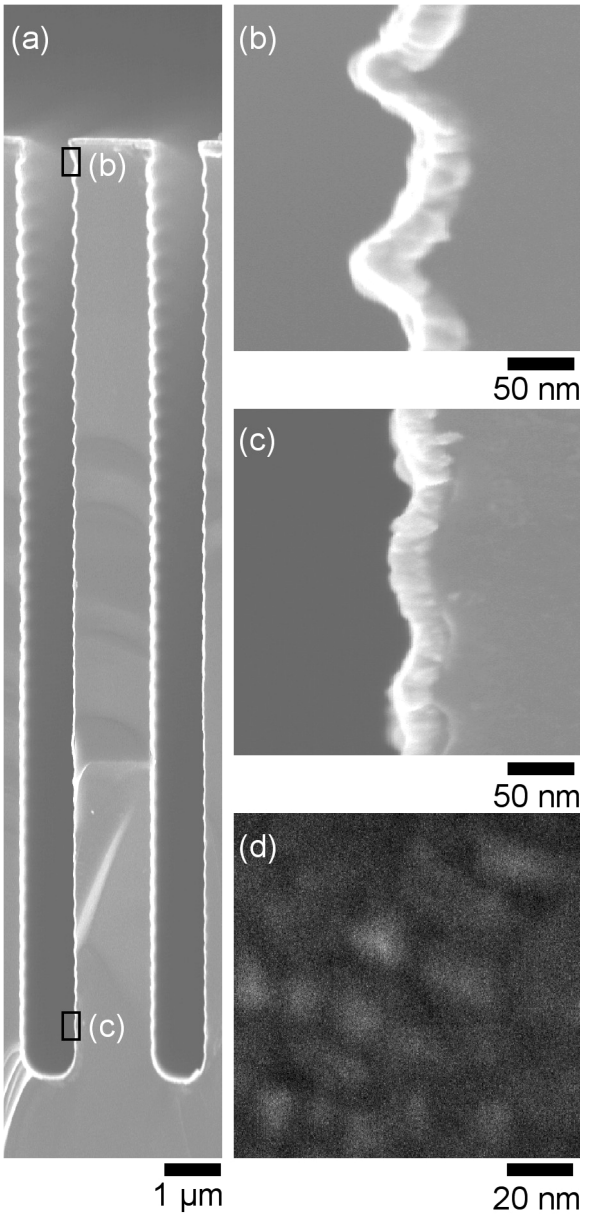

Figure 5. SEM images of an ALD mixed-metal film prepared using a $Ir(acac)_3$:$Pt(MeCp)Me_3$ cycles ratio of 1:1. In panel (a), the film conformally coats the trench structure with an aspect ratio of ~19. Panel (b) shows an enlarged view of the trench top. Panel (c) shows an enlarged view near the bottom of the trench. Panel (d) shows an SEM image of film surface morphology showing the typical granular texture.

for Ir ALD and Pt ALD, respectively. The agreement between the composition measurements for the Ir−Pt ALD mixed-metal films and the RoM prediction (see eq 6) supports the conclusion that both the Ir and Pt ALD are unaffected by the presence of the other metal. This predictability simplifies the process of achieving a specific film composition by adjusting the percentage of Ir cycles. We can employ the rule of mixtures as a predictive tool to tailor the alloy composition for specific applications. Although we did not explicitly measure the impurity content of our films, four-point-probe measurements yielded resistivity values that were consistent with oxygen-free metal films for the ALD Pt, ALD Ir, and mixed-metal samples.

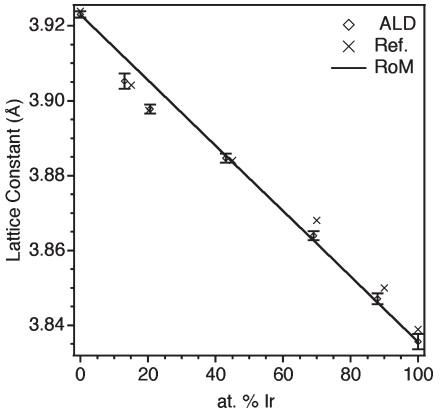

Figure 6. ALD film lattice constant, as a function of the iridium content (given in terms of at. %); the lattice constant transitions from that of platinum to iridium with increasing iridium content.

Alloy Film Morphology and Structure. The step coverage and conformality of the ALD Ir−Pt alloy films were evaluated using SEM images of a film with a thickness of 32.2 nm, as determined by XRF, prepared using an $Ir(acac)_3$:$Pt(MeCp)Me_3$ ratio of 1:1 on a silicon substrate with micromachined, high-aspect-ratio features (see Figure 5). Figure 5a shows the ALD Ir−Pt film over two adjacent trenches with an aspect ratio of ~19. Figures 5b and 5c show magnified images of the top and bottom of the left trench in Figure 5a. The Ir−Pt ALD film thickness is almost identical at the top (36 ± 3 nm) and bottom (31 ± 3 nm) of the trench, confirming that the process is conformal. Similar results were obtained from SEM images of ALD Ir−Pt alloy films prepared using other metal precursor ratios. This conformality for the Ir−Pt alloy films is consistent with previous studies for the pure ALD Ir[42] and ALD Pt[43] films.

Figure 5d shows a plan-view SEM image for the same ALD Ir−Pt alloy film as that shown in Figure 1. The granular morphology that is apparent in this image suggests a nanocrystalline film. By examining similar SEM images recorded from ALD Ir−Pt alloy films prepared with different $Ir(acac)_3$:$Pt(MeCp)Me_3$ dosing ratios (see the Supporting Information), we discovered that the film morphology is not appreciably dependent on the film composition and resembles other pure ALD noble metals.[33,34,44−46]

Our XRD studies indicate that all the ALD Ir−Pt alloy films deposited in the form of a face-centered cubic single-phase solid solution. The diffraction patterns and additional analysis are provided in the Supporting Information. One might expect the ALD Ir−Pt alloy films to possess a laminate structure that results from the layer-by-layer synthesis. The XRD data do not show features that are characteristic of a superlattice or other long-range ordering, although this phase may be difficult to distinguish from the bulk, because of the similarities in atom size, scattering contrast, and crystal structure.

(46) Christensen, S. T.; Elam, J. W.; Lee, B.; Feng, Z.; Bedzyk, M. J.; Hersam, M. C. Nanoscale Structure and Morphology of Atomic Layer Deposition Platinum on $SrTiO_3$ (001). *Chem. Mater.* **2009**, *21*(3), 516–521.

Figure 6 shows the lattice parameter deduced from the XRD data as a function of the measured iridium composition. The lattice constant for the pure ALD Pt film has a value of $a_{Pt} = 3.923$ Å. The lattice constant decreases monotonically as the iridium content increases, to a value of $a_{Ir} = 3.836$ Å for the pure Ir ALD film. The solid line in Figure 6 is based on the RoM formula:

$$a = (1 - f_{Ir})a_{Pt} + f_{Ir}a_{Ir} \quad (7)$$

Figure 6 also includes the lattice parameter values from the literature for similar bulk Ir−Pt compositions.[52]

It is instructive to compare our XRD results for the ALD Ir−Pt films with the existing literature for Ir−Pt bulk alloys. Bulk Ir−Pt alloys behave as a solid solution above ~1400 °C; however, below 1370 °C, a miscibility gap exists in the composition range of 35−90 at.% Ir. However, the literature does not provide information at the 300 °C deposition temperature used in our study. The XRD data indicate the presence of a single-phase solid solution. This establishes the fact that the platinum and iridium do not nucleate as separate grains of pure elements, because the diffractometer has sufficient resolution to discriminate between separate Pt and Ir phases. Interestingly, the ALD film lattice constant seems to agree well with alloys that have been prepared at significantly higher temperatures. Both the ALD films and the bulk alloys follow the rule of mixtures above 50 at.% Ir; however, the lattice parameter drops below the RoM predictions near 25 at.% Ir. This deviation has been reported elsewhere and was attributed to strain fields and attractive/repulsive interactions between the metal atoms.[47,48] The drop in lattice constant shown in Figure 6 may indicate an enhanced interaction between the Ir and Pt atoms, relative to the miscibility gap.

(47) Barrett, C. S. *Structure of Metals*; McGraw−Hill: New York, 1952.
(48) Tripathi, S. N.; Chandrasekharaiah, M. S. Thermodynamic Properties of Binary-Alloys of Platinum Metals. 2. Ir-Pt System. *J. Less-Common Met.* **1983**, *91*(2), 251–260.

Conclusions

The atomic layer deposition (ALD) of mixed-metal Ir−Pt layers has been explored using *in situ* quartz crystal microbalance (QCM) and quadrupole mass spectrometry (QMS), as well as *ex situ* scanning electron microscopy (SEM), X-ray fluorescence (XRF), and X-ray diffraction (XRD). The ALD Ir−Pt mixed-metal films deposit in a predictable manner, in which the growth rate, composition, and lattice parameter obey rule-of-mixtures formulas. XRD studies reveal that the ALD Ir−Pt mixed-metal films deposit as a single-phase, solid solution similar to previous reports of bulk Ir−Pt alloys prepared at higher temperatures. These results suggest that ALD may be a facile and general approach for preparing noble-metal alloy films and nanostructures for applications in catalysis, chemical sensors, microelectronics, corrosion resistance, medicine, and other fields.

Acknowledgment. This work was supported by the U.S. Department of Energy, Office of Energy Efficiency and Renewable Energy, Industrial Technologies Program (under Contract No. YN-19-01-000). X-ray measurements were performed at the DuPont−Northwestern−Dow Collaborative Access Team (DND-CAT) located at Sector 5 of the Advanced Photon Source (APS). DND-CAT is supported by E.I. DuPont de Nemours & Co., The Dow Chemical Company, and the State of Illinois. The electron microscopy was performed at the Electron Microscopy Center for Materials Research (EMCMR) at Argonne National Laboratory. Use of the APS and EMCMR was supported by the U.S. Department of Energy, Office of Science, Office of Basic Energy Sciences (under Contract No. DE-AC02-06CH11357, operated by UChicago Argonne, LLC). Additional X-ray measurements made use of Northwestern University Central Facilities supported by the Materials Research Science and Engineering Center (through National Science Foundation Contract No. DMR-0520513).

Supporting Information Available: This material is available free of charge via the Internet at http://pubs.acs.org.